A 750-MHz electronically tunable resonator using microstrip line couplers for electron paramagnetic resonance imaging of a mouse tumor-bearing leg

Tatsuya Amida, Ririko Nakaoka, Denis A. Komarov, Kumiko Yamamoto, Osamu Inanami, Shingo Matsumoto, Hiroshi Hirata*

Abstract*—*Objective: **The purpose of this work was to develop an electronically tunable resonator operating at 750 MHz for continuous-wave electron paramagnetic resonance (CW-EPR) imaging of a mouse tumor-bearing leg.** ***Methods:*** **The resonator had a multi-coil parallel-gap structure with a sample space of 16 mm in diameter and 20 mm in length. Microstrip line couplers were used in conjunction with varactor diodes to enable resonance frequency adjustment and to reduce the non-linear effects of the varactor diodes. The resonator was modeled by the finite-element method and a microwave circuit simulation was performed to clarify its radiofrequency characteristics.** ***Results:*** **A tunable resonator was evaluated in terms of its resonance frequency, tunable frequency band, and conversion efficiency of the RF magnetic field. The developed resonator provided a tunable frequency band of 4 MHz at a central frequency of 747 MHz and a conversion efficiency of 34 $\mu T/W^{1/2}$. To demonstrate the application of this tunable resonator to EPR imaging, three-dimensional EPR images of a sample solution and a mouse tumor-bearing leg were obtained.** ***Conclusion:*** **The developed tunable resonator satisfied our initial requirements for *in vivo* EPR imaging and may be able to be further improved using the present finite-element and circuit models if any problems arise during future practical applications.** ***Significance:*** **This work may help to promote EPR imaging of tumor-bearing mice in cancer-related studies.**

***Index Terms*—Coils, couplers, electromagnetic waves, electron paramagnetic resonance, magnetic resonance imaging, radiofrequency.**

Manuscript received May 21, 2017; revised July yy, 2017. First published xxx yy, 2017. This work was supported by JSPS KAKENHI grant number 26249057 and 16K12862. *Asterisk indicates corresponding author.*

T. Amida was with the Division of Bioengineering and Bioinformatics, Graduate School of Information Science and Technology, Hokkaido University, Sapporo, Japan (e-mail: amida.tatsuya@gmail.com).

R. Nakaoka, D. A. Komarov, S. Matsumoto, and *H. Hirata are with the Division of Bioengineering and Bioinformatics, Graduate School of Information Science and Technology, Hokkaido University, North 14, West 9, Kita-ku, Sapporo, 060-0814, Japan (r.nakaoka@ist.hokudai.ac.jp; dkomarov@ist.hokudai.ac.jp; smatsumoto@ist.hokudai.ac.jp; hhirata@ist.hokudai.ac.jp).

K. Yamamoto and O. Inanami are with Laboratory of Radiation Biology, Graduate School of Veterinary Medicine, Hokkaido University, North 18, West 9, Kita-ku, Sapporo, 060-0818, Japan (e-mail: k_yamamoto@vetmed.hokudai.ac.jp; inanami@vetmed.hokudai.ac.jp).

I. Introduction

VISUALIZATION of the microenvironment of tumor tissues is important for understanding their pathophysiological status and their response to treatments [1]. Tumor tissues often have a low oxygen content, which makes them resistant to radiation therapy [2,3]. The oxygen partial pressure can be measured by electron paramagnetic resonance (EPR) using oxygen-sensitive free radical molecules called spin probes [4–7]. For better penetration of electromagnetic waves into biological tissues, relatively low magnetic fields (8 to 42 mT) and the corresponding frequencies of electromagnetic waves in the range of 250 MHz to 1.2 GHz are used for EPR spectroscopy and imaging in small animals [8]. Optimization of a radiofrequency (RF) resonator is always desirable for a specific application of EPR. In animal studies of radiation therapy and oncology, tumor cells are often implanted in hind legs of mice [9,10]. Therefore, an RF resonator should be able to accommodate a tumor-bearing leg.

The stability of EPR signal acquisition is also important for the study of tumors because motion of a subject animal may cause a significant reflection of RF electromagnetic waves at the RF resonator and degrade the signal-to-noise ratio (SNR) of EPR spectra. For continuous-wave (CW) EPR spectroscopy and imaging, an RF resonator with a high quality factor is desirable for improving the EPR signal sensitivity [11]. The RF characteristics of a resonator with a high quality factor are sensitive to the motion of the subject animal. Thus, voltage-controlled frequency adjustment of either the RF resonator or the RF signal source in an EPR reflection-type bridge should be useful for compensating for perturbations caused by the motion of an animal in the EPR resonator.

Several approaches to controlling the resonance frequency have been reported in the context of *in vivo* EPR spectroscopy and imaging. Frequency adjustment has been achieved by changing the capacitance in the RF resonator through the movement of a dielectric substrate with an induction motor [12] or a piezoelectric actuator [13], and through the use of varactor diodes [14–16]. The use of induction motors or piezoelectric actuators requires high stability of the movement of mechanical elements in the resonator. On the other hand,

while a varactor diode-based tuning approach does not require the movement of mechanical elements, with this approach, the frequency of the resonator can only be tuned within a limited range. To take the limited range of varactor diodes into account, an appropriate model of a tunable resonator is necessary when the resonator is designed for EPR imaging. In addition, the non-linear effects of varactor diodes on the tunable resonator should be reduced [17]. A tunable resonator that uses microstrip line couplers for CW-EPR imaging has not yet been discussed. Therefore, a model of a tunable resonator for a mouse tumor-bearing leg should be established.

The purpose of this work was to develop an electronically tunable resonator operating at 750 MHz for CW-EPR imaging of a mouse tumor-bearing leg. To solve the technical problem of non-linear effects of varactor diodes, we used microstrip line couplers to remove frequency-tuning varactor diodes from the RF transmission line of the resonator, which should reduce the non-linear effects of the resonator. The resonator structure and numerical modeling using a microwave field simulator and microwave circuit simulator are described. A multi-coil parallel-gap resonator (MCPGR) was used in our design in conjunction with microstrip line couplers and varactor diodes to enable frequency adjustment. The MCPGR is a modified form of a lumped element resonator, such as a loop-gap resonator or a split-ring resonator [18–20]. MCPGRs have been successfully used for CW-EPR imaging at 650 and 750 MHz [21,22]. To support our model of a tunable resonator, the characteristics of the physically constructed resonator were compared to the results of a computer simulation. Finally, application of the developed resonator to EPR imaging of a sample solution and tumor-bearing mice is demonstrated.

II. Design and Evaluation Methods

A. Design requirements

Several requirements must be considered in the design of a tunable resonator for CW-EPR imaging of tumor-bearing mice. (i) The resonance frequency of the resonator has to be in the range of 740 to 760 MHz. This is because the static magnetic field in our EPR spectrometer is generated by permanent magnets of 27 mT. Thus, an RF frequency of approximately 750 MHz is required for EPR detection of paramagnetic species with a *g*-factor of 2 (most organic radicals). The central value of the magnetic field can be adjusted somewhat by the use of field scanning coils. (ii) The resonance frequency of the tunable resonator should be able to be controlled by the application of a reverse-bias voltage to varactor diodes. Our CW-EPR spectrometer has an automatic tuning control (ATC) system that allows us to adjust the resonance frequency of the RF resonator to the frequency of the incident RF waves [23,24]. To enable negative feedback control of the resonance frequency, it should be possible to change the resonance frequency of the resonator over a range of several MHz. This would enable ATC to compensate for perturbations of the resonance frequency caused by the motion of a subject animal. A shift in the resonance frequency due to tumor growth can be compensated by tuning the carrier frequency of the RF synthesizer that corresponds to a shift in the magnetic field. The tunable band of 4 MHz allows ATC to compensate for the shift in resonance frequency due to the motion of an animal during EPR data acquisition. (iii) To improve the sensitivity of EPR detection, a higher conversion efficiency of the RF magnetic field is desirable [25]. (iv) The MCPGR should be able to accommodate a mouse tumor-bearing hind leg. In our previous study, tumor volumes reached approximately 1.5 cm^3 10 or 11 days after the implantation of squamous cell carcinoma (SCC) [26]. Taking this into account, we chose an inner diameter of 16 mm and a length of 20 mm for the MCPGR. (v) Finally, the sample space of the resonator has to be upright for easy animal handling in our experiments.

B. Structure of the resonator

Figure 1(a) illustrates the structure of a tunable resonator that uses microstrip line couplers. The MCPGR consists of three conductive loops connected to a copper-clad dielectric substrate, capacitors connected in series between the dielectric substrate and the coaxial lines, a parallel transmission line formed by two coaxial lines, microstrip line couplers, varactor diodes for adjusting the resonance frequency and impedance-matching of the resonator, and a half-wave line balun made of a coaxial line. Tin-plated copper wires (18 British Standard Wire Gauge, thickness of the wire was 1.2 mm) were connected to the copper-clad polytetrafluoroethylene (PTFE) dielectric substrate (0.38 mm in thickness, CuFlon® 15-7-7, Polyflon Company, Norwalk, CT) as shown in Fig. 1(b). An equivalent circuit of the MCPGR composed of three loops and a dielectric substrate is shown in Fig. 1(c). While there are many combinations of the number of coils and capacitance C_p, three coils were suitable to make the resonance frequency approximately 750 MHz with the 0.38-mm CuFlon® substrate. When more coils are used, a greater capacitance can be achieved through the use of a very thin dielectric substrate. For ease of handling, a 0.38-mm CuFlon® substrate was chosen for the MCPGR.

The capacitors C_s were made with a 0.25-mm thick PTFE substrate (CuFlon® 10-7-7). Fifty-ohm non-magnetic semi-rigid coaxial lines (5.0 mm in diameter, 207 mm in length, SC-500/50, COAX Company, Yokohama, Japan) were used for the parallel transmission line. The length of the transmission line was determined by a $\lambda/4$-impedance transform for the MCPGR and extension of the line ($\lambda/2$, no impedance transform) that would keep the tuning and matching circuits away from the field modulation coils (described in section II-D).

The microstrip line coupler structure was composed of a 1.27-mm-thick microwave substrate with dielectric constant ε_r 10.2 and dissipation factor $\tan\delta$ 0.0022 (RO3010™, Rogers Corp., Rogers, CT). The use of microstrip line couplers was intended to reduce the RF power applied to the varactor diodes for frequency tuning. Varactor diodes (BB181, NXP Semiconductors, Eindhoven, Netherlands) were connected to the ends of the coupler lines to enable adjustment of the resonance frequency. Another pair of varactor diodes (1SV217, Toshiba, Tokyo, Japan) was used to adjust the impedance of

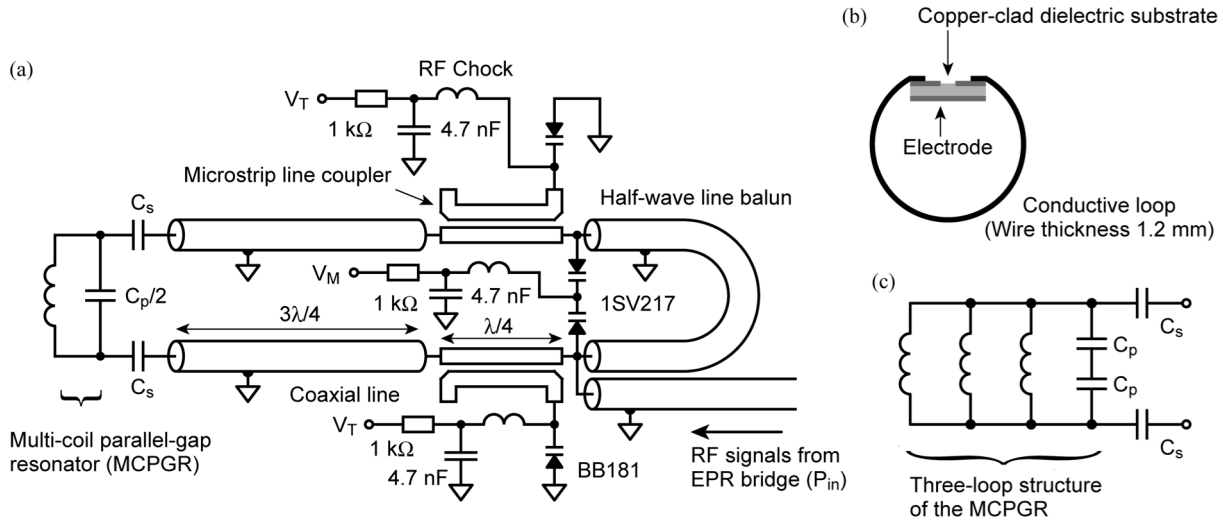

Fig. 1. Schematic diagram of the electronically tunable resonator. (a) Configuration of a tunable resonator with microstrip line couplers, (b) structure of the multi-coil parallel-gap resonator (MCPGR), and (c) equivalent circuit of the MCPGR with three conductive loops.

the resonator. Reverse-bias voltages for tuning and matching adjustment were applied to varactor diodes through RF choke coils. The half-wave line balun was made of a 50-ohm non-magnetic semi-rigid coaxial line (2.2 mm in diameter, 138 mm in length, SC-219/50-SC, COAX Corporation, Yokohama, Japan).

Figure 2 shows a cross-section of the tunable resonator. The MCPGR was held with a cylindrical sleeve made of cross-linked polystyrene (REXOLITE® 1422, C-Lec Plastics Inc., Philadelphia, PA). The inner and outer diameters of the sleeve were 16 and 18 mm, respectively. The MCPGR was placed in the RF shield made of REXOLITE® and covered with strips of copper foil (50 μm in thickness, 10 mm in width). The inner and outer diameters of the shield were 38 and 40 mm, respectively. This RF shield suppresses unwanted radiation from the MCPGR and allows the penetration of magnetic field modulation at 90 kHz to the sample. The position of the RF shield is not symmetric with respect to the MCPGR to make it easier to access the sample space and to provide an open area for the body of a subject mouse.

C. *Modeling of the resonator*

The characteristics of the tunable resonator were computed using an HFSS 3-D full-wave microwave field simulator (version 13.0.0) and the Designer environment (version 6.1.0) by ANSYS Inc. (Canonsburg, PA). The tunable resonator was modeled on the basis of a previous report regarding a 1.1-GHz surface-coil resonator for EPR tooth dosimetry [27]. Figure 3(a) shows a three-dimensional (3D) finite-element model of the MCPGR. For simplicity, Fig. 3(a) does not show the RF shield made of strips of copper foil, although the shield was included in the finite-element model. The space of 120 mm × 120 mm × 120 mm was modeled with a radiation boundary condition. The MCPGR was placed in the center of the space. Microstrip line couplers on the microwave substrate were

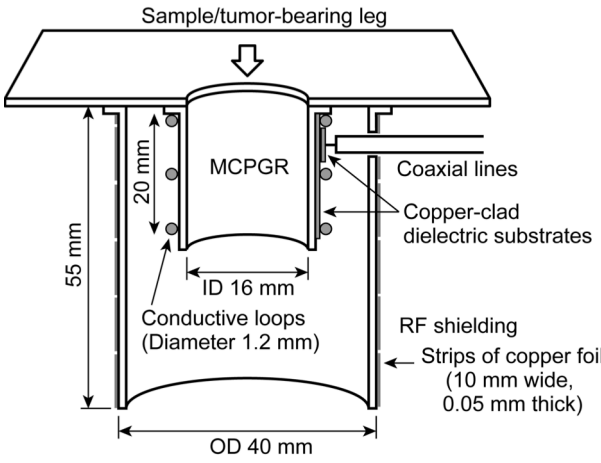

Fig. 2. Cross-section of the multi-coil parallel-gap resonator (MCPGR) and the RF shield.

modeled with HFSS as presented in Fig. 3(b). The geometry and sizes of the couplers are given in Fig. 3(c). The width of microstrip lines (1.2 mm) was chosen to achieve an impedance of 50 Ω. Coaxial lines were modeled with Q3D Extractor (version 10.0.0, ANSYS). Figure 3(d) presents the whole model of the tunable resonator built in the Designer environment. The solution converged in our simulation. To calculate the conversion efficiency in our simulation, the generated RF magnetic field at the center of the MCPGR was divided by the square root of the input RF power P_{in} to the resonator. In our calculations, the input RF power P_{in} was 1 W. Thus, the RF magnetic field (in Tesla) is directly related to the conversion efficiency in units of $T/W^{1/2}$.

To compare the simulated and measured RF characteristics, the scattering-matrix parameter S_{11} of the tunable resonator was measured with a vector network analyzer (E5062A, Keysight Technologies, Santa Rosa, CA).

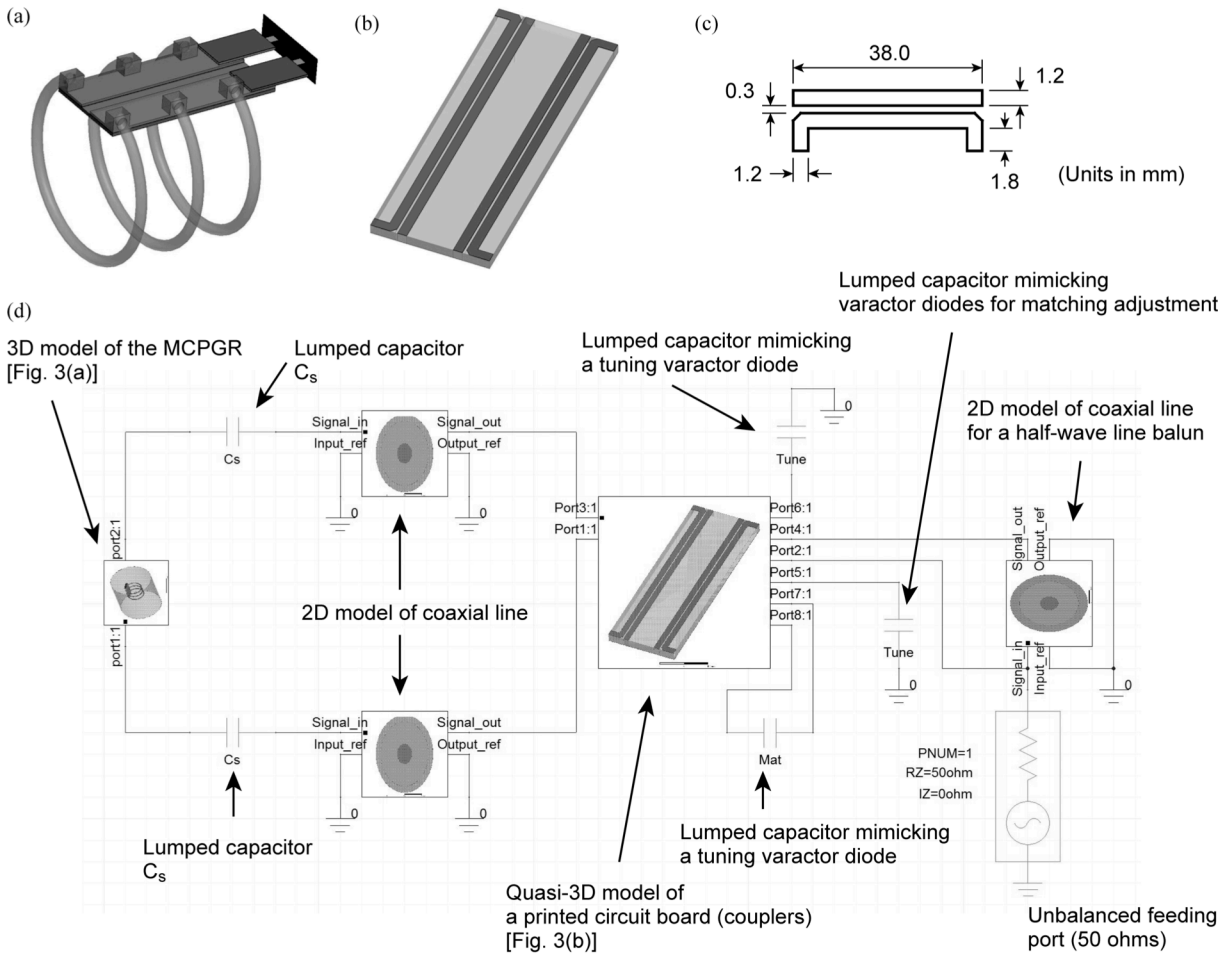

Fig. 3. Modeling of the tunable resonator. (a) Three-dimensional (3D) models of the MCPGR, (b) 3D model of microstrip line couplers on a printed circuit board, and (c) the geometry of the microstrip line couplers (not depicted proportional to the actual sizes of the couplers). Models constructed with the finite-element method (FEM) for electromagnetic field simulation were built with an ANSYS HFSS electromagnetic wave simulator. (d) RF circuit modeling of the tunable resonator in the ANSYS Designer environment.

D. Construction of the resonator and magnetic field modulation coils

After we simulated the RF characteristics of the resonator, the tunable resonator was physically constructed to evaluate its RF characteristics and EPR imaging. The microstrip line couplers, varactor diodes, reverse-bias circuits, and the half-wave line balun were contained in a copper shield box (5 mm in thickness) to reduce interference with magnetic field modulation at 90 kHz. A Helmholtz coil pair with an inter-coil distance of 50 mm and a mean diameter of 100 mm was used for magnetic field modulation. The coils were made on 1.6-mm-thick glass-reinforced epoxy laminate sheets (model no. 34, Sunhayato Corp., Tokyo, Japan, equivalent of FR-4). The MCPGR and the RF shield were attached to a 1-mm-thick Bakelite plate, which in turn was attached to the modulation coils.

E. EPR imaging of a sample solution

To examine the developed tunable resonator for 3D EPR imaging, a sample of radical solution was visualized with a CW-EPR-based single-point imaging (SPI) protocol [28–30]. For the imaging experiments, the developed tunable resonator was installed into the magnet of a laboratory-built 750-MHz CW-EPR spectrometer/imager. The details of the CW-EPR spectrometer/imager have been reported previously [31,32]. Nitroxyl radical, *trans*-3,4-dicarboxy-2,2,5,5-tetra($^2H_3$)methylpyrrolidin-(3,4-$^2H_2$)-(1-^{15}N)-1-oxyl (^{2}H,^{15}N-DCP), was used as the imaging probe [33]. The ^{2}H,^{15}N-DCP radical was synthesized and kindly provided by Dr. Igor A. Kirilyuk, Novosibirsk Institute of Organic Chemistry, Novosibirsk, Russia. The radical was dissolved in phosphate-buffered saline (PBS) and the pH was adjusted to 7.4. An Eppendorf microcentrifuge tube containing 1.3 mL 3 mM ^{2}H,^{15}N-DCP radical solution was placed into the MCPGR. Note that the length of the tube (40 mm) was greater than the height of the MCPGR (20 mm). Thus, the bottom of the tube was outside of the sensitive region of the resonator. For EPR image-acquisition, the central magnetic field was adjusted to the absorption peak at a lower magnetic field (^{2}H,^{15}N-DCP shows two absorption peaks). The measurement parameters of EPR imaging were as follows: scan time 100 ms, magnetic field scanning 1.5 mT, magnetic field modulation 60 μT, modulation frequency 90 kHz, time-constant of a lock-in amplifier 100 μs, number of data acquisition points 512 per

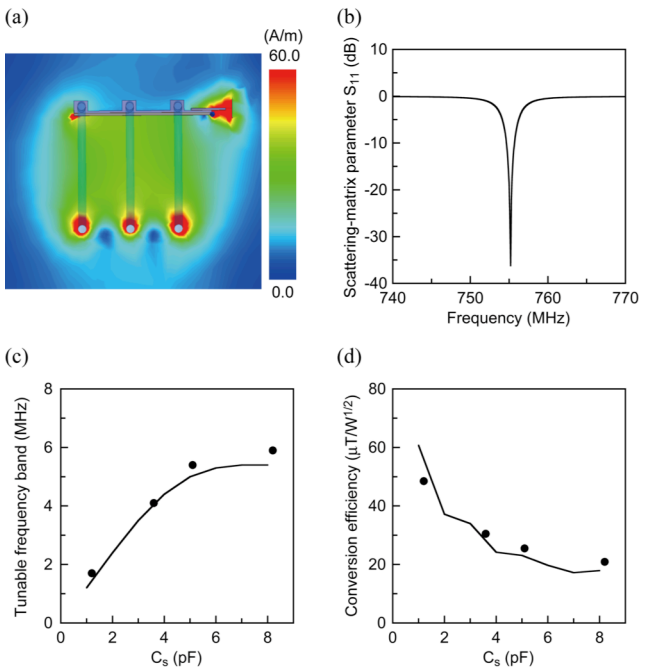

Fig. 4. Simulated results of RF characteristics of the tunable resonator. (a) The RF magnetic field at the center of the MCPGR when an RF power of 1 W was applied to the feeding port of the tunable resonator, (b) reflection characteristics (scattering-matrix parameter S_{11}) of the tunable resonator (C_s 3.5 pF), (c) tunable frequency band as a function of coupling capacitor C_s, and (d) the conversion efficiency of the RF magnetic field as a function of coupling capacitor C_s. In Fig. 4(c) and (d), solid lines show the simulated results for the tunable frequency bands and the conversion efficiencies. Closed plots show the experimental results for the tunable frequency bands and the conversion efficiencies.

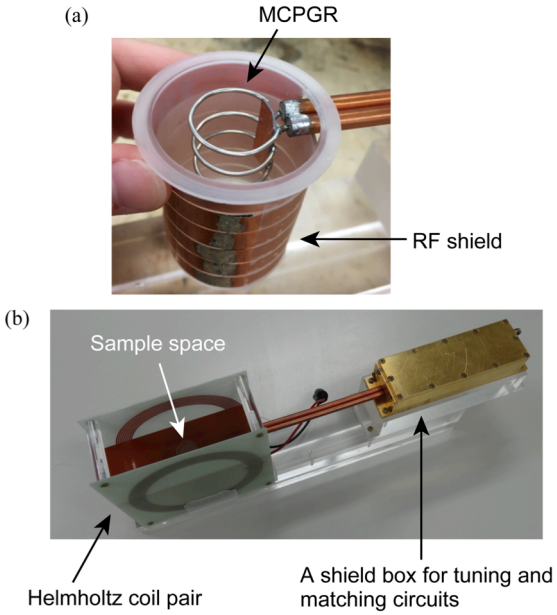

Fig. 5. Photographs of a 750-MHz tunable resonator. (a) The MCPGR and RF shield, and (b) the tunable resonator and a Helmholtz coil pair.

scan, and incident RF power 14 mW. Incrementally ramped field gradients in equal steps were used for EPR image-acquisition. The projections were acquired at 15 × 15 ×15 field gradients for the X-, Y-, and Z-directions (total of 3375 projections). The maximum field gradient for each direction was 30 mT/m. Two sets of projection data were accumulated to improve the SNR of the resulting EPR images. The total image-acquisition time was 15 min.

F. In vivo EPR imaging

Three tumor-bearing mice were prepared to demonstrate *in vivo* EPR imaging with the developed resonator. The details of animal preparation have been reported previously [34]. In brief, six-week-old C3H/HeJ male mice were purchased from Japan SLC (Hamamatsu, Japan). Murine squamous cell carcinoma (SCC VII) cells [35] were subcutaneously injected into the right hind leg. The cells were cultured as previously reported [34]. *In vivo* EPR imaging of tumor-bearing mice was performed 6 days after the implantation of SCC VII cells. At that time, the mice body weights were 20 to 21 g and the tumor volumes were approximately 0.6 cm^3. The tumor-bearing hind leg of an anesthetized mouse was placed into the MCPGR. The imaging probe $^2H,^{15}N$-DCP was intravenously injected as a bolus (1.5 mmol/kg body weight) into a subject mouse through a tail vein. EPR data-acquisition was started 5 minutes after the injection and a total of 3375 projections were acquired over the next 7.5 minutes. In our previous study, we showed that this acquisition scheme ensures a high intensity for the EPR signal and a steady concentration of $^2H,^{15}N$-DCP radical in the tumor tissue [34]. The incident RF power for imaging of a tumor-bearing mouse leg was 23 mW. The other EPR settings were similar to those in imaging of the sample solution. All experiments were performed in accordance with the 'Law for The Care and Welfare of Animals in Japan' and were approved by the Animal Experiment Committee of Hokkaido University (approval no. 15-0120).

III. Results and Discussion

A. Simulation of resonance characteristics and RF magnetic field

The tunable resonator model presented in Fig. 3 was used for calculations of the RF magnetic field distribution and the scattering-matrix parameter S_{11}. Figure 4(a) shows the simulated distribution of the RF magnetic field inside the MCPGR. Figure 4(b) shows scattering-matrix parameter S_{11} for the tunable resonator under the conditions of coupling capacitance C_s 3.5 pF, capacitance mimicking matching varactor diodes 6.0 pF, and capacitance mimicking tuning varactor diodes 11.0 pF. A resonance peak was observed at 755 MHz with no other spurious peaks in the vicinity. A solid line in Fig. 4(c) shows the tunable frequency band as a function of coupling capacitance C_s. As can be seen from Fig. 4(c), the tunable frequency band increased with an increase in the coupling capacitance and reached a plateau at C_s > 6 pF. The tuning varactor diode connected to the coupler behaves like a capacitor connected in series to the capacitor C_s. Therefore, a small value of C_s reduces the influence of the varactor diode on the resonance frequency, and this results in a decrease in the tunable frequency band. The conversion efficiency for the resonator was calculated from the RF

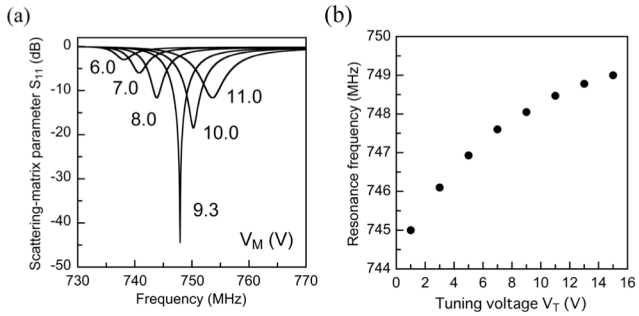

Fig. 6. Resonance characteristics of the tunable resonator. (a) Scattering-matrix parameter S_{11} as a function of matching control voltage V_M, and (b) the resonance frequency as a function of tuning control voltage V_T.

magnetic flux density at the center of the MCPGR. The solid line in Fig. 4(d) shows the simulated conversion efficiency of the RF magnetic field as a function of coupling capacitance C_s. The conversion efficiency increased when the coupling capacitance C_s decreased. The influence of coupling capacitance C_s on the conversion efficiency is due to a change in the transmission coefficient from the parallel transmission line to the MCPGR. A few bumps were seen in the solid line of the conversion efficiency due to alterations in the resonance frequency caused by changes in the coupling capacitance C_s. While the capacitance C_p of the MCPGR can be adjusted to keep the resonance frequency constant by changing the dimensions of the dielectric substrate, we made an allowance for the resonance frequency in the range of 740 to 760 MHz. As can be seen in Figs. 4(c) and 4(d), the conversion efficiency of the RF magnetic field can be increased with a sacrifice of the tunable frequency band. If the perturbation of the resonance frequency due to animal motion is not problematic, a smaller value of coupling capacitance C_s can be used to achieve a higher conversion efficiency of the RF magnetic field and to improve the EPR signal sensitivity.

B. RF characteristics of the tunable resonator

To verify our modeling of the tunable resonator, we physically constructed the tunable resonator, as shown in Fig. 5, based on the above-mentioned design and simulated results. The dimensions of the copper-clad dielectric substrate in the MCPGR (see Fig. 1(b)) were 10 mm × 20 mm × 0.38 mm, and the electrodes were made by partially removing a copper foil on the substrate. The capacitance C_p (Fig. 1(c)) was 3.9 pF. The coupling capacitance C_s was chosen to be 3.0 pF. Measured insertion loss and coupling of a fabricated microstrip line coupler at 750 MHz were 0.36 dB and 12.2 dB, respectively. Thus, only 6 % of the RF power flowing in the main line of the coupler is applied to the varactor diode for frequency tuning. We think that this small fraction of the RF power in the coupler reduced the non-linear effects of the varactor diodes. When the varactor diodes and transmission lines were connected in series, the received signal with twice the frequency of FM modulation for ATC phase-sensitive detection was distorted (data not shown). However, the received signal showed a less-distorted sinusoidal signal with the tunable resonator using microstrip line couplers.

The resonance frequency and the tunable frequency band of the physically constructed resonator were compared to the simulated results. Figure 6(a) shows the scattering-matrix parameter S_{11} of a physically constructed tunable resonator with various matching-control voltages V_M. The reflection characteristics exhibited a resonance peak around 750 MHz, as we designed. Critical coupling of the resonator at 748.6 MHz was observed at a matching-control voltage of 9.3 V. For the constructed resonator, the unloaded quality factor was 190, and the conversion efficiency of the RF magnetic field was 34 $\mu T/W^{1/2}$. The metal perturbing sphere method was used to obtain the conversion efficiency [36,37]. Figure 6(b) shows the measured resonance frequency as a function of the tuning-control voltage V_T. From 1 V to 15 V, the resonance frequency shifted from 745 MHz to 749 MHz (4 MHz). This tunable band satisfies the specifications given above. The tunable frequency band and the conversion efficiency of the RF magnetic field were measured with four different coupling capacitors C_s. Closed plots in Fig. 4(c) and Fig 4(d) show the measured values of the tunable frequency band and the conversion efficiency, respectively. As can be seen in Figs. 4(c) and 4(d), the measured parameters are in good agreement with the simulated results, which validates the numerical modeling of the tunable resonator. For the constructed resonator, the unloaded quality factor was approximately 380 when coupling capacitance C_s was 1.0 pF. A quality factor of 190 was measured when C_s was 3.0 pF, as mentioned above. Thus, the quality factor and the conversion efficiency can be increased by decreasing C_s. However, smaller C_s did not provide the desired tunable frequency band.

A previously reported 750-MHz tunable resonator (24 mm in inner diameter, 30 mm in length) for a mouse head had a conversion efficiency of 42 $\mu T/W^{1/2}$ [32]. Although smaller loops were used in the present resonator, the conversion efficiency of the resonator was slightly less than that of the previous resonator. There are three explanations for why the present resonator had a lower conversion efficiency: (i) use of a quasi-open RF shield, (ii) a longer transmission line between the MCPGR and the matching circuitry, and (iii) a trade-off relationship between the conversion efficiency and the tunable frequency band. For RF shielding, one end of the MCPGR is open to the ambient space in contrast to the 100-mm long RF shield of the previous resonator (see Figs. 2 and 5). Therefore, the radiation of electromagnetic waves to the ambient space increases the loss of the resonator. The longer transmission line stores more RF energy than that in the previous resonator. This decreases the RF energy in the MCPGR. Also, the conversion efficiency was sacrificed to achieve the target tunable frequency band in the present resonator (see Fig. 4).

C. EPR imaging of a sample solution

EPR imaging of a sample solution was performed with the developed tunable resonator. Figures 7(a) and 7(b) show the chemical structure of the $^{2}H,^{15}N$-DCP imaging probe and its first-derivative EPR absorption spectrum measured with the developed tunable resonator. Figures 7(c) and 7(d) show a

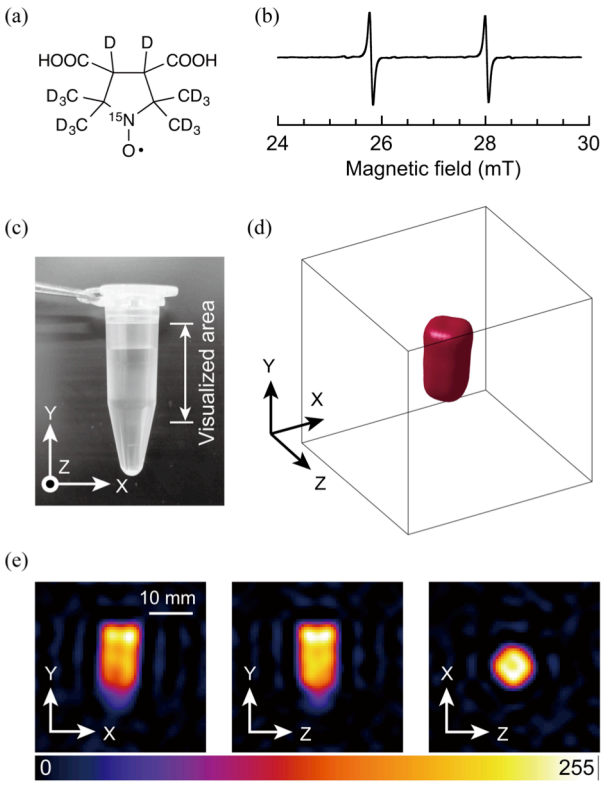

Fig. 7. Three-dimensional EPR imaging of a sample solution. (a) Chemical structure of ^{2}H,^{15}N-DCP, (b) first-derivative EPR absorption spectrum of ^{2}H,^{15}N-DCP, (c) photograph of the sample tube containing 3 mM ^{2}H,^{15}N-DCP radical solution (1.3 mL), (d) surface-rendered image of the sample solution, and (e) slice-selective EPR intensity maps. The field-of-view (FOV) of the 3D image is 39 mm × 39 mm × 39 mm in Fig. 6(d), and the image matrix size is 64 × 64 × 64.

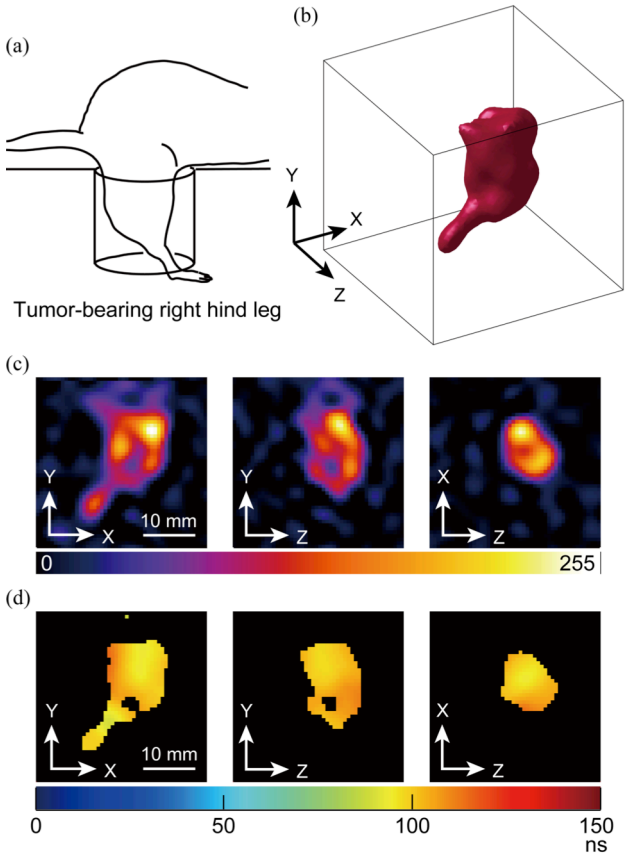

Fig. 8. Three-dimensional EPR imaging of a mouse tumor-bearing leg. (a) Illustration of the mouse tumor-bearing leg in the MCPGR, (b) surface-rendered image of EPR signals in the tumor-bearing leg, (c) slice-selective EPR intensity maps, and (d) transverse relaxation time T_2^* maps corresponding to the intensity maps in Fig. 8(c). The FOV of the 3D image in Fig. 8 is 33 mm × 33 mm × 33 mm, and the image matrix size is 48 × 48 × 48.

photograph and the surface-rendered EPR image for ^{2}H,^{15}N-DCP solution in the tube, respectively. A threshold of 30% of the maximum signal intensity in the 3D data was applied to a process of surface rendering. Figure 7(e) shows the slice-selective EPR signal intensity maps generated from the 3D image data. The bottom part of the tube was not visualized because it was outside the sensitive region of the MCPGR. No significant distortion of the reconstructed image was observed.

While the solution of the imaging probe was uniform in the tube, some intensity variations were observed in EPR intensity maps in Fig. 7(e). The EPR signal intensity profile depends on several factors such as inhomogeneity of the RF magnetic field, the spatial resolution of an EPR image, and eddy currents in a conductive sample solution. The areas at the top and bottom edges of the MCPGR have a lower intensity of the RF magnetic field. Also, the limited spatial resolution of the image makes the edge of the sample solution a blurred profile. In addition, since PBS is a conductive medium, eddy currents are generated and suppress the RF magnetic field in the solution. These factors influence the EPR signal intensity and help to vary the intensity over the image.

D. In vivo EPR imaging of a mouse tumor-bearing leg

Tumor-bearing mice were scanned to demonstrate *in vivo* EPR imaging with the tunable resonator. When a tumor-bearing leg (tumor volume 0.6 cm^3) was placed in the MCPGR, the loaded quality factor was 120 and the shift in the resonance frequency was less than 0.1 MHz.

Figure 8(a) illustrates the arrangement of a tumor-bearing hind leg in the resonator. Figure 8(b) shows the surface-rendered image of EPR signals in the tumor-bearing leg. Figures 8(c) and 8(d) show slice-selective maps of the EPR intensity and relaxation time T_2^*, respectively. A 30% threshold of the maximum signal intensity was applied to surface rendering and T_2^* mapping.

The results shown in Fig. 8 confirm that the developed tunable resonator could be used for *in vivo* EPR imaging of a mouse tumor-bearing leg. The ^{2}H,^{15}N-DCP imaging probe exhibits very low toxicity [34] and none of the subject mice in our experiments died. Nevertheless, the lowest possible dose of imaging agent is always preferable for animal studies. Optimization of the experimental conditions and improvement of the conversion efficiency of the RF magnetic field may be able to further improve the EPR signal sensitivity and allow a decrease in the dose of the imaging probe.

A region of low signal intensity in the tumor-bearing leg is

shown in Fig. 8(c), and results in a void of T_2^* data in Fig. 8(d). This observation can be explained by taking into account the fact that fast-growing tumors typically have underdeveloped vasculature and delivery of the imaging probe to the tumor tissue by blood flow is hindered. Relaxation time T_2^* is sensitive to the oxygen partial pressure as well as to the concentration of the imaging probe. The T_2^* maps can be converted to oxygen partial pressure maps if we account for the influence of the concentration on T_2^*. While we did not convert T_2^* maps to oxygen partial pressure in this paper, this will be a subject for future studies. Mouse tumor-bearing legs have been measured in a vertical orientation in previous studies of *in vivo* EPR imaging [10,29,30]. Physiological problems regarding a vertical orientation of the legs have not been reported.

From a technical point of view, ATC could work with the tunable resonator during EPR image-acquisition. Critical coupling of the resonator was obtained without any difficulties. This suggests that the second or higher harmonics of reflected RF waves caused by the non-linearity of varactor diodes have a negligible impact on RF signal reflection in the developed tunable resonator.

IV. Conclusion

A 750-MHz tunable resonator was designed and tested for CW-EPR imaging of tumor-bearing mice. The developed tunable resonator satisfied our initial requirements for *in vivo* EPR imaging and may be able to be further improved using the present finite-element and circuit models if any problems arise during future practical applications. The introduction of microstrip line couplers to the tunable resonator avoided any difficulties in achieving critical coupling of the resonator. The present resonator may promote EPR imaging of tumor-bearing mice in cancer-related studies.

Acknowledgment

The nitroxyl radical probe used in this study was kindly provided by Dr. Igor A. Kirilyuk, Novosibirsk Institute of Organic Chemistry, Novosibirsk, Russia.

References

[1] K. Brindle, "New approaches for imaging tumour responses to treatment," *Nat. Rev. Cancer*, vol. 8, no. 2, pp. 94–107, Feb. 2008.

[2] M. R. Horsman, "Measurement of tumor oxygenation," Int. J. Radiat. Oncol. Biol. Phys., vol. 42, no. 4, pp. 701–704, Nov. 1998.

[3] M. Höckel *et al*., "Association between tumor hypoxia and malignant progress in advanced cancer of the uterine cervix," *Cancer Res*., vol. 56, no. 19, pp. 4509–4515, Oct. 1996.

[4] K. J. Liu *et al*, "Lithium phthalocyanine: A probe for electron paramagnetic resonance oximetry in viable biological systems," *Proc. Natl. Acad. Sci. USA*, vol. 90, no. 12, pp. 5438–5442, June 1993.

[5] H. J. Halpern *et al*., "Oxymetry deep in tissues with low-frequency electron paramagnetic resonance," *Proc. Natl. Acad. Sci. USA*, vol. 91, no. 26, pp. 13047–13051, Dec. 1994.

[6] J. L. Zweier and P. Kuppusamy, "Electron paramagnetic resonance measurements of free radicals in the intact beating heart: a technique for detection and characterization of free radicals in whole biological tissues," *Proc. Natl. Acad. Sci. USA*, vol. 85, no. 15, pp. 5703–5707, Aug. 1988.

[7] R. P. Pandian *et al*., "Novel particulate spin probe for targeted determination of oxygen in cells and tissues," *Free Radic. Biol. Med.*, vol. 35, no. 9, pp. 1138–1148, Nov. 2003.

[8] G. R. Eaton and S. S. Eaton, "EPR Spectrometers at Frequencies below X-band," in *Biological Magnetic Resonance Vol. 21 EPR: Instrumental Methods*, C. J. Bender and L. J. Berliner, Eds. New York, Kluwer Academic/Plenum Publishers, 2004, pp. 50–114.

[9] M. Elas *et al*., "Electron paramagnetic resonance oxygen images correlate spatially and quantitatively with Oxylite oxygen measurements," *Clin. Cancer Res.*, vol. 12, no. 14, pp. 4209-4217, July 2006.

[10] S. Matsumoto *et al*., "Low-field paramagnetic resonance imaging of tumor oxygenation and glycolytic activity in mice," *J. Clin. Invest.*, vol. 118, no. 5, pp. 1965–1973, May 2008.

[11] G. Feher, "Sensitivity Considerations in Microwave Paramagnetic Resonance Absorption Techniques," Bell System Tech. J., vol. 36, no. 2, pp. 449-484, Mar. 1957.

[12] J. A. Brivati *et al*, "A radiofrequency ESR spectrometer for in vivo imaging," *J. Magn. Reson.*, vol. 92, no. 3, pp. 480–489, May 1991.

[13] M. Chzhan *et al*, "Development of an electronically tunable L-band resonator for EPR spectroscopy and imaging of biological samples," *J. Magn. Reson. B*, vol. 108, no. 1, pp. 67–72, July 1995.

[14] H. Hirata *et al*., "Electronically tunable surface-coil-type resonator for L-band EPR spectroscopy," *J. Magn. Reson*., vol. 142, no. 1, pp. 159–167, Jan. 2000.

[15] G. He *et al*., "Development of a resonator with automatic tuning and coupling capability to minimize sample motion noise for in vivo EPR spectroscopy," *J. Magn. Reson.*, vol. 149, no. 2, pp. 218–227, Apr. 2001.

[16] T. Walczak *et al*., "L-band electron paramagnetic resonance spectrometer for use in vivo and in studies of aqueous biological samples," *Rev. Sci. Instrum.*, vol. 76, no. 1, 013107, Jan. 2005.

[17] H. Hirata *et al*., "Characteristics of an electronically tunable surface-coil-type resonator for L-band electron paramagnetic resonance spectroscopy," *Rev. Sci. Instrum.*, vol. 72, no. 6, pp. 2839-2841, June 2001.

[18] W. N. Hardy and L. A. Whitehead, "Split-ring resonator for use in magnetic resonance from 200-2000 MHz," *Rev. Sci. Instrum*., vol. 52, no. 2, pp. 213–216, Feb. 1981.

[19] W. Froncisz and J. S. Hyde, "The loop-gap resonator: a new microwave lumped circuit ESR sample structure," *J. Magn. Reson*., vol. 47, pp. 515–521, 1982.

[20] M. Mehdizadeh *et al*., "Loop-gap resonator: a lumped mode microwave resonant structure," *IEEE Trans. Microwave Theory Tech*., vol. MTT-31, no. 12, pp. 1059–1064, Dec. 1983.

[21] Y. Kawada *et al*., "Use of multi-coil parallel-gap resonators for co-registration EPR/NMR imaging," *J. Magn. Reson.*, vol. 184, no. 1, pp. 29–38, Jan. 2007.

[22] H. G. Fujii *et al*., "Noninvasive mapping of the redox status in septic mouse by in vivo electron paramagnetic resonance imaging," *Magn. Reson. Imaging*, vol. 31, no. 1, pp. 130–138, Jan. 2013.

[23] H. Hirata *et al*., "Detection of electron paramagnetic resonance absorption using frequency modulation," *J. Magn. Reson.*, vol. 164, no. 2, pp. 233–241, Oct. 2003.

[24] H. Hirata *et al*., "Decoupling of automatic control systems in a continuous-wave electron paramagnetic resonance spectrometer for biomedical applications," *NMR Biomed.*, vol. 17, no. 5, pp. 295–302, Aug. 2004.

[25] G. R. Eaton *et al*., "Resonator Q," in *Quantitative EPR*, Wien, Austria, Springer, 2010, pp. 79–90.

[26] J. Goodwin *et al*., "In vivo tumour extracellular pH monitoring using electron paramagnetic resonance: the effect of X-ray irradiation," *NMR Biomed.*, vol. 27, no. 4, pp. 453–458, Apr. 2014.

[27] H. Sugawara *et al*., "Design and evaluation of a 1.1-GHz surface coil resonator for electron paramagnetic resonance-based tooth dosimetry," *IEEE Trans. Biomed. Eng.*, vol. 61, no. 6, pp. 1894–1901, June 2014.

[28] S. Subramanian *et al*., "Single-point (constant-time) imaging in radiofrequency Fourier transform electron paramagnetic resonance," *Magn. Reson. Med*., vol. 48, no. 2, pp. 370–379, Aug. 2002.

[29] K. Matsumoto *et al*., "Application of continuous-wave EPR spectral-spatial image reconstruction techniques for in vivo oxymetry: comparison of projection reconstruction and constant-time modalities," *Magn. Reson. Med*., 50, no. 4, pp. 865–874, Oct. 2003.

[30] H. Jang *et al*., "Single acquisition quantitative single-point electron paramagnetic resonance imaging," *Magn. Reson. Med*., vol. 70, no. 4, pp. 1173–1181, Oct. 2013.

[31] H. Sato-Akaba *et al*., "Improvement of temporal resolution for three-dimensional continuous-wave electron paramagnetic resonance imaging," *Rev. Sci. Instrum*., vol. 79, no. 12, 123701, Dec. 2008.

[32] H. Sato-Akaba *et al*., "Half-life mapping of nitroxyl radicals with three-dimensional electron paramagnetic resonance imaging at an interval of 3.6 seconds," *Anal. Chem*., vol. 81, no. 17, pp. 7501–7506, Sept. 2009.

[33] A. A. Gorodetsky *et al*., "Functional electron paramagnetic resonance imaging of ischemic rat heart: Monitoring of tissue oxygenation and pH," *Magn. Reson. Med*., vol. 76, no. 1, pp. 350–358, Jan. 2016.

[34] H. Kubota *et al*., "Feasibility of in vivo three-dimensional T_2^* mapping using dicarboxy-PROXYL and CW-EPR-based single-point imaging," *Magn. Reson. Mater. Phy.*, 2017. doi: 10.1007/s10334-016-0606-8.

[35] H. D. Suit and C. Suchato, "Hyperbaric oxygen and radiotherapy of a fibrosarcoma and of a squamous-cell carcinoma of C3H mice," Radiology, vol. 89, no. 4, pp. 713–719, Oct. 1967.

[36] L. C. Maier Jr and J. C. Slater, "Field strength measurements in resonant cavities," *J. Appl. Phys.*, vol. 23, no. 1, pp. 68–77, Jan. 1952.

[37] J. H. Freed *et al*., "Theory of saturation and double resonance effects in ESR spectra: III rf coherence and line shapes," *J. Chem. Phys.*, vol. 47, no. 8, pp. 2762–2773, Oct. 1967.